

Harnessing Stratospheric Diffusion Barriers for Enhanced Climate Geoengineering

Nikolas O. Aksamit¹, Ben Kravitz^{2,3}, Douglas G. MacMartin⁴, George Haller¹

¹Institute for Mechanical Systems, Swiss Federal Institute of Technology (ETH), Zürich, Switzerland.

²Department of Earth and Atmospheric Sciences, Indiana University, Bloomington, IN, USA.

³Atmospheric Sciences and Global Change Division, Pacific Northwest National Laboratory, Richland, WA, USA.

⁴Sibley School of Mechanical and Aerospace Engineering, Cornell University, Ithaca, NY, USA.

Correspondence to: Nikolas O. Aksamit (naksamit@ethz.ch)

Abstract. Stratospheric sulfate-aerosol geoengineering is a proposed method to temporarily intervene in the climate system to increase reflectance of shortwave radiation and reduce mean global temperature. In previous climate modeling studies, choosing injection locations for geoengineering aerosols has thus far only utilized average dynamics of stratospheric wind fields instead of accounting for the essential role of time-varying material transport barriers in turbulent atmospheric flows. Here we conduct the first analysis of sulfate aerosol dispersion in the stratosphere comparing a now-standard fixed-injection scheme with time-varying injection locations that harness short-term stratospheric diffusion barriers. We show how diffusive transport barriers can quickly be identified and we provide an automated injection location selection algorithm using short forecast and reanalysis data. Within the first seven days of transport, the dynamics-based approach is able to produce particle distributions with greater global coverage than fixed-site methods with fewer injections. Additionally, this enhanced dispersion slows aerosol microphysical growth, reducing the effective radii of aerosols at monthly timescales. This has long term impacts on radiative forcing, beyond the lifespan of the original influential transport barriers. We conclude that previous feasibility studies of geoengineering likely underestimate the potential cooling efficiency of sulfate aerosol geoengineering by not strategically injecting at optimized dispersion locations.

Deleted: inform optimal

Deleted: locations

Deleted: increasing lifespan

Deleted: sulfate

Deleted: and yearly

1 Introduction

Stratospheric sulfate-aerosol geoengineering relies on triggering an atmospheric perturbation through deliberate injections of sulfate aerosol precursors (often SO₂) into the lower stratosphere to mimic the cooling effects seen after large volcanic eruptions [The Royal Society, 2009]. Over the last several decades, this has been suggested as a possible means of reducing some of the impacts of climate change [e.g., Crutzen, 2006]. There are, however, many open questions about the effects of radiative forcing from sulfate injections [Kravitz and MacMartin, 2020]. The importance of choosing the altitude and latitudes of injection, and distribution of injection rates across those, has been clearly demonstrated, as well as adjusting injection locations based on the season [Visioni et al., 2020]. Additionally, even for sulfate aerosols, the method of dispersal will affect aerosol size distribution, and hence the amount of material that needs to be injected. To date, many of these uncertainties are

Deleted: the seasons of

Deleted: [cite].

Deleted: aerosol

40 based on a climate response from fixed-injection locations [e.g. Robock et al., 2008; Heckendorn et al., 2009; Tilmes et al.,
 41 ~~fully turbulent fluid~~ 2017], a significant limitation for predicting dispersion in ~~fully turbulent fluid~~ flows. In fact, none of these studies consider the
 42 short-term variations of stratospheric winds or the organizing role of turbulent coherent structures in these time-varying flows.
 43 Driscoll et al. [2012] showed that it is impossible to correctly capture the impact of abrupt atmospheric perturbations on
 44 surface climate without a well-resolved stratospheric model. With the great significance of stratospheric dynamics for
 45 teleconnections and the state of the atmosphere [e.g. Jaiser et al., 2013; Domeisen et al., 2018], how can we optimize where to
 46 put aerosols or precursors so that we have greater influence on the mean climate, and with better efficiency?
 47 While benchmark studies have been quite successful at understanding the mean climatic response of geoengineering in
 48 sophisticated Earth System Models [e.g. Kashimura et al., 2017; Kravitz et al., 2017], the injection protocols have all neglected
 49 presently-available short-term predictive information useful for optimizing particle dispersion. An efficient dispersion of
 50 aerosol precursors is of crucial importance for aerosol coagulation [Kravitz and MacMartin, 2020]: the particle size
 51 distribution is a critical and sensitive parameter for accurately determining surface cooling, stratospheric warming, and changes
 52 in stratospheric dynamics [e.g., Rasch et al., 2008; Heckendorn et al., 2009; Tilmes et al., 2008; Niemeier et al., 2011]. By
 53 only considering ~~average flow behavior~~, one limits geoengineering evaluations to simple injection protocols that do not fully
 54 exploit turbulence, coherence, and mixing in the stratosphere. This increases the likelihood of a heterogeneous spatial coverage
 55 and localized high concentrations of aerosols, leading to enhanced coagulation and sedimentation rates [e.g., Pierce et al.,
 56 2010]. Without a more precise optimization of injection locations, we limit our ability to accurately model ~~the~~ full potential
 57 impacts of geoengineering.

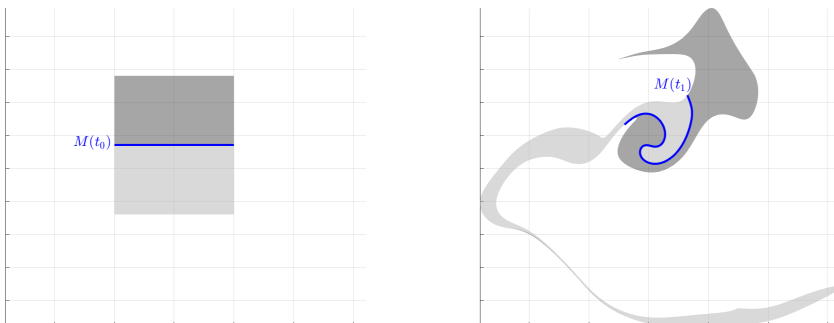
Deleted: time-varying

Deleted: however,

Deleted: *<object>*

Deleted: mean

Deleted: or



60 **Figure 1: Example of fluid particle advection for an unsteady geophysical 2D fluid flow from time t_0 to time t_1 .** For
 any arbitrary line of initial fluid particle positions, such as $M(t_0)$, that line will be a barrier to advective transport and
 mixing. This is seen in the second panel as no dark grey fluid has crossed $M(t_1)$ to mix with the light grey fluid.

Instead of standard fixed-locations, we propose a time-varying injection location protocol based on identification and prediction of short-term Lagrangian stratospheric transport barriers. This method harnesses the theory of Lagrangian coherent structures (LCSs), a tool for highlighting the most influential material surfaces solely from fluid velocity fields without any further modeling of scalar transport [Haller, 2015]. For a given unsteady fluid flow, any arbitrary surface of fluid particles, M , will block advective transport across that surface over time as the surface deforms with the flow. This is shown in a [real](#) 2D velocity field of geostrophic ocean surface currents in Figure 1. Here, the blue line M separates regions of light and dark grey fluid particles. As the fluid flows from time t_0 to t_1 , M is an advective transport barrier in that no dark grey fluid crosses M to mix with the light grey fluid. This result follows immediately from the continuity of the equations defining fluid motion.

Instead of looking for material barriers to advective transport, of which there are infinitely many, LCS theory identifies only exceptional distinguished material surfaces, such as those that are mathematically defined to be rotationally coherent, undergo minimal stretching over time, or locally attract or repel nearby fluid particles at a significant rate. One example of the latter two structures, termed hyperbolic LCS, and their time evolution in the same unsteady ocean flow are shown in Figure 2. Over the time period t_0 to t_2 , M_A is the structure that is mathematically-defined to most effectively attract nearby particles, and M_R repels nearby particles. By identifying exceptional material barriers, such as the saddle feature in Figure 2, LCS theory allows organization of turbulent fluid flows into coherent patterns in a mathematically-rigorous (non-empirical), physical and frame-independent manner [Haller, 2015].

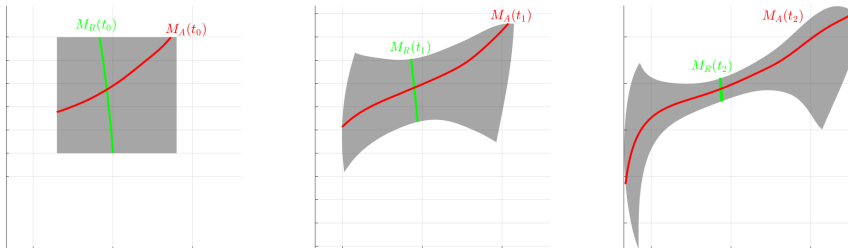


Figure 2: Example of time evolution of fluid particles surrounding hyperbolic LCS in a geophysical fluid flow from time t_0 to t_2 . M_A is an attracting LCS (unstable-manifold) and M_R is a repelling LCS (stable-manifold).

Though [using](#) the mathematical definition of [LCS](#) to define atmospheric flow structures [is quite](#) restrictive, LCS have actually been identified throughout the atmosphere [Tang et al., 2010; Tallapragada et al., 2011; Rutherford et al., 2012; BozorgMagham and Ross, 2015; Knutson et al., 2015; Wang et al., 2017]. Of particular relevance to the present research is the LCS work of Beron-Vera et al. [2012] who demonstrated how zonal jets behave as meridional transport barriers at high latitudes. Olascoaga et al. [2012] analyzed LCS in stratospheric winds to provide a rigorous definition of the transport barriers

Deleted: M

Deleted: 4

Deleted: <object>

Deleted: as LCS

contributing to the loss of ozone from the Arctic ozone layer, and there was recent success in delineating LCS along atmospheric rivers [Garaboa-Paz et al., 2015]. Jupiter's Great Red Spot and zonal jets were identified as material transport barriers through video analysis and LCS theory [Hadjighasem and Haller 2016]. Using a null-geodesic identification scheme, the northern polar vortex, a significant structure in high-latitude atmospheric mixing, was accurately identified as a transport-blocking LCS [Serra et al., 2017]. Lastly, Wang et al. [2017] were able to use a related diagnostic strain-tensor field to predict the location of space shuttle contaminant plumes in the thermosphere after 48 hours of transport. These previous results indicate the potential for the most influential LCS to be harnessed for geoengineering purposes. Specifically, hyperbolic LCS that maximize or minimize dispersion may be used as time-varying injection locations that reduce coagulation of aerosols and increase their lifespan and utility.

105 Recently, Haller et al. [2018, 2020] derived an additional objective criterion that specifically identifies the strongest barriers and enhancers of diffusive particle transport. That is, one can identify the time-varying locations of material barriers in a fluid flow that maximize or minimize the diffusive contribution in the advection-diffusion equations over a given timeframe. They have obtained a diffusion barrier strength (DBS) field whose ridges highlight the strongest diffusive transport barriers in forward-time fluid flow analysis and strongest diffusive transport enhancers by running a backward-time fluid flow analysis.

110 Neither of these simulations actually require modeling the evolution of a diffusive scalar field, but still rigorously define the structures that are most influential to diffusive transport. For atmospheric science, this significantly reduces the computational burden for predicting how scalar fields will evolve as it provides quantitative information about future attraction and dispersion patterns without needing complex numerical machinery to model the advection-diffusion equations, or making assumptions about their unknown initial- and boundary conditions. In comparison, the effective-diffusivity approach of Nakamura [2008]

115 provides an a-posteriori visualization of Eulerian barriers, but only after scalar transport simulations have been performed. DBS fields, however, give an a priori (predictive) characterization of material barriers to diffusion without ever running diffusive simulations. This new technique increases the rigor of Lagrangian atmospheric analysis and removes ambiguity arising from the lack of a universal definition of coherence in atmospheric LCS work. As such, the DBS field is perfectly suited for optimizing aerosol dispersion and is computable solely from available wind field forecasts and hindcasts or 120 reanalysis.

In this manuscript, we evaluate simulated stratospheric flows with the aim of identifying diffusive transport barriers and informing injection site selection for enhanced stratospheric geoengineering via aerosols. In doing so, we provide an initial demonstration of the benefits of incorporating short-term atmospheric dynamics into geoengineering analyses and provide suggestions to better assess its potential impacts. Our choice of dynamics-informed injections is evaluated against fixed-125 injection protocols via long-term metrics of pure advective transport, and for geoengineering scenarios simulated in a fully coupled climate-model. We find significant improvement in the ability of injected aerosols to both quickly surround the earth, and to be able to achieve similar coverage with fewer injection sites. We then introduce further practical and logistical restrictions on the DBS-based protocol, and maintain our method's improved performance.

Deleted: moving

Deleted: in

Deleted: , without

Deleted:

Deleted: fields

Deleted: achieve geoengineering objectives over the standard methods.

2 Methods

2.1 Climate Model Data

We use CESM2 (WACCM6) [Gettelman et al., 2019] under an SSP5-8.5 scenario to generate global wind fields at 72 levels for 18.75 years of simulation (Table 1). These fields were computed at a spatial resolution of 0.94° latitude and 1.25° longitude,

140 with instantaneous output at 6-hour frequency. As vertical motion is minimized over short timescales along isentropic surfaces, and similar analysis has reliably identified transport barriers along these surfaces [Serra et al., 2017], we extracted wind fields on isentropes ranging from T=280 K to 1000 K with 20 K resolution. This is expected to provide a computationally efficient 2D analysis of material barriers to aerosol and tracer transport. We primarily focus on the T=540 K isentrope in the lower stratosphere (approximately 20-25 km ASL in the tropics) as these elevations are at the upper limit of currently practical aerosol injection heights. The DBS-injection protocols described herein rely only on 14-day windows of wind velocity and can be applied to wind data at any height. It is reasonable to assume that applying these methods elsewhere and optimizing injection locations to maximize dispersion at other heights would be beneficial for aerosol global coverage and similar results may be possible.

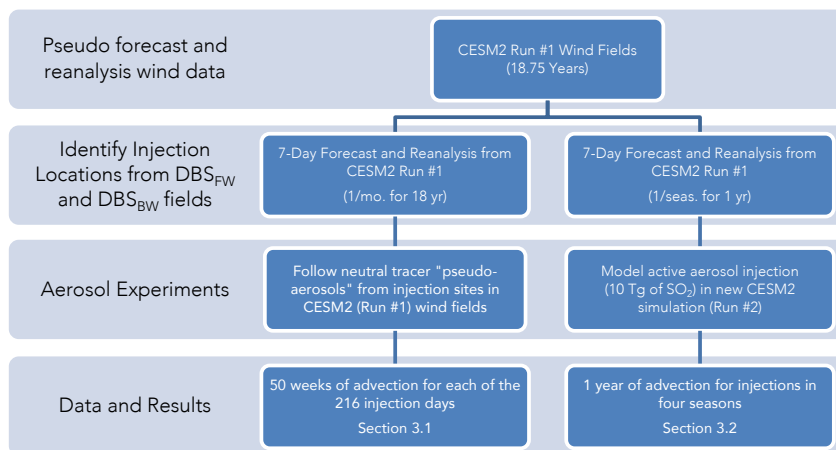
Deleted: ..

Deleted: on

Deleted: along

Deleted: particle

Deleted: The fundamental differences we find between the DBS-injection and fixed-injection protocols are, however, relevant for any height



150 **Figure 3: Flow chart for geoengineering experiments**

A preliminary dispersion analysis was first conducted by approximating aerosol concentration evolution from the behavior of neutral tracers that perfectly follow the wind fields (Figure 3, left column). At the beginning of each month for the full 18.75 years of CESM2 (WACCM6) model simulation, injection locations were identified using a short temporal neighborhood of

Deleted: modeling aerosols as non-reactive fluid-particles.

Deleted: defined

the wind-field output from CESM2 (WACCM6) [Run #1](#). The advection of parcels of neutral tracers from neighborhoods 165 surrounding those injection points was then computed for the [following 50 months in the Run #1 wind fields](#). This approximation of aerosol transport by perfectly fluid-following particles inherently assumes that there are negligible inertial effects and the aerosol vertical motion is not influenced by radiative heating or cooling of the particle. While these assumptions limit any study of climate impacts, these calculations provide a longitudinal [comparison of dispersion from dynamics-informed injections](#) and [traditional injection protocols that spans multiple modes of interannual climate variability](#).

170 We complement our [neutral tracer](#) trajectory analysis with [four comprehensive CESM2 \(WACCM6\) simulations spanning one-year after sulfate precursor injection](#) ([Figure 3, right column](#)). [Each simulation corresponds with injections during a particular season](#). These simulations incorporate the advection of aerosols with full microphysics, atmospheric chemistry and radiative forcing components, [as well as all other earth system model components](#). Again, the performance of DBS-informed and fixed-location sites are compared. As the inclusion of microphysics and atmospheric chemistry makes these simulations 175 computationally more expensive, [no further improvements to injection site selection methods were evaluated, though several suggestions for future work are discussed in the discussion and conclusions](#).

Deleted:).
Deleted: dense
Deleted: fluid particles
Deleted: next week
Deleted: study
Deleted: injection dispersion spanning numerous natural climate cycles
Deleted: allows comparison with
Deleted: basic fluid-particle
Deleted: a
Deleted: simulation suite of one-year
Deleted: with
Deleted: occurring
Deleted: each
Deleted: with
Deleted: the subsequent evolution of each injection is only computed for one calendar year after injection
Formatted: Font: Bold, English (US)
Formatted: Left

2.2 Lagrangian transport extremizers

Diffusion Barrier Strength (DBS) is an objective (i.e. observer-independent) diagnostic field whose ridges highlight diffusive 180 or stochastic transport extremizers from velocity data [Haller et al., 2018]. For a given time-varying velocity field $\mathbf{v}(\mathbf{x}, t)$, and tracer $c(\mathbf{x}, t)$ we can describe the evolution of this tracer with the classic advection-diffusion equation:

$$\frac{\partial c}{\partial t} + \nabla \cdot (\mathbf{c}\mathbf{v}) = \mathbf{v}\nabla \cdot (\mathbf{D}\nabla c), \quad c(\mathbf{x}, t_0) = c_0(\mathbf{x}),$$

where $\mathbf{D}(\mathbf{x}, t)$ is the symmetric, positive definite diffusion-structure tensor. The left-hand-side of this differential equation contains the advection of this scalar field whereas the right-hand-side describes transport due to diffusive processes.

185 Furthermore, we define the path of a fluid particle in the velocity field $\mathbf{v}(\mathbf{x}, t)$ as a solution to the ordinary differential equation $\dot{\mathbf{x}} = \mathbf{v}(\mathbf{x}, t)$, described by the flow map:

$$\mathbf{F}_{t_0}^t(\mathbf{x}_0) = \mathbf{x}(t, t_0, \mathbf{x}_0).$$

From here, we define the DBS at a point \mathbf{x}_0 over the time interval $[t_0, t_1]$ as

$$DBS(\mathbf{x}_0) = \text{trace } \bar{\mathbf{T}}_{t_0}^{t_1}(\mathbf{x}_0),$$

190 where overbar denotes the time-average of the transport tensor.

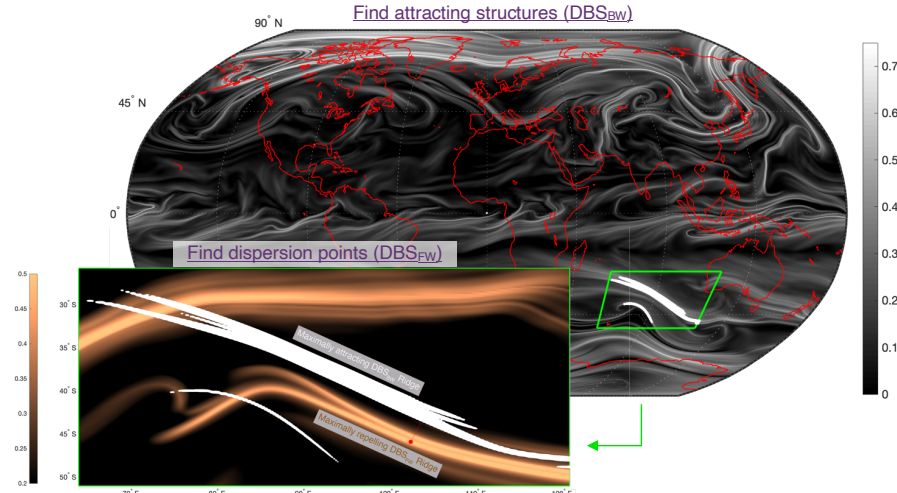
$$\mathbf{T}_{t_0}^t(\mathbf{x}_0) = [\nabla \mathbf{F}_{t_0}^t]^{-1} \mathbf{D}(\nabla \mathbf{F}_{t_0}^t, t) [\nabla \mathbf{F}_{t_0}^t]^{-1},$$

Deleted: [T^t_{t₀}\(x₀\) = \[∇F^t_{t₀}\]⁻¹D\(∇F^t_{t₀}, t\) \[∇F^t_{t₀}\]⁻¹, over \[t₀](#)

for $t \in [t_0, t_1]$.

The diffusion-structure tensor \mathbf{D} is capable of representing parameterizations of many complex diffusion-like processes, but our research focuses on molecular (i.e. homogeneous, isotropic and steady) diffusion, in which case $\mathbf{D}(\mathbf{x}, t)$ is constantly the

identity matrix. In this situation, the transport tensor $\mathbf{T}_{t_0}^t$ reduces to the inverse of the Cauchy-Green strain tensor, $\mathbf{C}_{t_0}^t = \mathbf{I}$, 215 $[\nabla \mathbf{F}_{t_0}^t]^\top \nabla \mathbf{F}_{t_0}^t$, that also arises in the computation of the Finite-Time Lyapunov Exponent (FTLE) used in previous atmospheric transport barrier studies [see, e.g., Beron-Vera et al., 2012; Olascoaga et al., 2012; Garoba-Paz et al., 2015; Serra et al., 2017; Wang et al., 2017]. DBS values are, therefore, pointwise equal to the trace of the time-averaged $[\mathbf{C}_{t_0}^t]^{-1} = [\nabla \mathbf{F}_{t_0}^t]^{-1} [\nabla \mathbf{F}_{t_0}^t]^\top$ tensor. One notable difference between DBS and FTLE is the inclusion of diffusive or stochastic transport in the definition of 220 transport barriers or enhancers for DBS, a process essential to predicting aerosol dispersion in the stratosphere. The inclusion of diffusion in the transport functional allows for a systematic search for extremizing surfaces to transport [Haller et al., 2018], thereby eliminating the ambiguity inherent in various available coherent structure definitions [see Haller, 2015], or a lack of 225 precisions from simple heuristics. Accounting for diffusive and stochastic transport necessarily leads to the inclusion of $\mathbf{C}_{t_0}^t$ tensors for all $t \in [t_0, t_1]$ in the definition of the DBS. In contrast, computing the FTLE only includes the single tensor $\mathbf{C}_{t_0}^{t_1}$.



225 **Figure 4: Example of DBS-informed injection scheme at 540K that selects the injection sites. The global view shows** seven-day DBS_{BW} fields with two sections of disconnected strongly attracting structures highlighted in the green box. **For the larger structure, we then identify all points closer to that attracting structure and select the unique point that** will result in the most significant dispersion of aerosols. **This is injection site is shown as the red dot on the DBS_{FW} ridge** in the inset. Injecting aerosols at these points will cause them to both spread quickly and converge to a large and 230 complex attractor. Units for both forward and backward DBS fields are day⁻¹.

Deleted: $\mathbf{T}_{t_0}^{t_1}$
Deleted: $\mathbf{C}_{t_0}^{t_1} = [\nabla \mathbf{F}_{t_0}^t]^\top$

Deleted: $[\mathbf{C}_{t_0}^{t_1}]^{-1}$
Deleted: $]$
Deleted: $\mathbf{C}_{t_0}^t$

Using a limited time-window of the modelled wind flow for DBS calculations, we were able to effectively simulate a real-time geoengineering scenario. For each injection time, t_0 , in our 18.75 years of simulation (Run #1), we analyzed one week of future flow data and one week of previous flow data as proxies for forecast and reanalysis, respectively, to determine optimal locations for sulfate injection. The one-week DBS_{FW} field was calculated from t_0 to $t_0 + 7$, and under reversal of the direction of the flow in the reanalysis data, the DBS_{BW} field was calculated from t_0 to $t_0 - 7$. As is described by Haller et al. [2018], the ridges of DBS_{FW} highlight locations of strongest dispersion (i.e. diffusive transport limiters) on the globe at t_0 , while the ridges of DBS_{BW} indicate the locations of the strongest accumulation (i.e. diffusive transport enhancers) at t_0 . These diffusive transport barriers are analogous to the structures M_A and M_R from Figure 2, but account for diffusive as well as advective transport in the flow. To identify DBS ridges, we advected fluid particles along isentropic surfaces to simplify calculations and ignored vertical motions.

We identified strongly attracting flow features as connected components of the DBS_{BW} field with values above a simple fixed threshold. This threshold was chosen empirically from the range of DBS values in these calculations and was constant for all structure identification at all t_0 . As also seen for other objective coherent structures identified from short-term calculations [e.g., Serra and Haller, 2016], these seven-day attracting features persist for much longer than their domain of computation in the flow and continue to attract many nearby fluid particles. Near each strongly attracting feature, the location with the largest DBS_{FW} value signals a potential injection site for geoengineering as it indicates the strongest local dispersion over the next seven days. We balance strong dispersion and nearby strong attractors to both maximize the spread of aerosols and to prevent multiple injections being attracted to the same sections of the same attractor. When possible, this methodology prevented aerosols injected at initially distant sites from traveling great distances only to be attracted to the same portion of the flow. A flow chart detailing the injection-location selection process is shown in Figure 4.

While we prioritize injecting near unique attractors, this was not always possible given that single DBS_{BW} ridges could also span much of the globe, and in rare instances strong attractors were not present in all regions. If seven unique attractors are not available at a given time, we simplify the process and choose the maximal DBS_{FW} site near an attractor for each of seven latitude bands: $[-7.5^\circ, 7.5^\circ]$, $[\pm 7.5^\circ, \pm 22.5^\circ]$, $[\pm 22.5^\circ, \pm 37.5^\circ]$, $[\pm 37.5^\circ, \pm 62.5^\circ]$. This dynamics-based injection approach, referred to as DI in the text, adapts to any isentrope or future climate scenario as the injection location choice always depends on the state of the stratosphere at the time of injection. This automated search algorithm is summarized in Table 1.

DBS-Enhanced Aerosol Injection Location Search Algorithm

Input: Wind fields surrounding injection day (t_0) from $t_0 - 7$ to $t_0 + 7$ days.

- 1) Calculate reanalysis DBS_{BW} from t_0 to $t_0 - 7$, and forecast DBS_{FW} from t_0 to $t_0 + 7$.
- 2) Extract attracting ridges as connected components of DBS_{BW} field above a fixed threshold via flood-fill algorithms.
- 3) Find seven largest ridges, and identify all points that are closer to each ridge than any other ridge.

Deleted: At the beginning of
Deleted: month during
Deleted:,
Deleted: That is, on a given day t_0 , the

Deleted:

Deleted: Figure 3: Example flow chart of DBS-informed injection scheme from 360K to highlight the selection process for a more complex flow. Clockwise from top left: Calculate seven-day DBS_{BW} field and identify strongly attracting connected flow-structures above a certain threshold; Identify the points closest to each attracting structure and choose a unique strongest seven-day DBS_{FW} (repelling) point for each attracting structure; injecting aerosols at these points will cause them to spread quickly and converge to dominant attracting structures.

Deleted: also

Deleted: regions

Deleted: 3

Deleted:

Deleted: Thus, we also allowed seeding near separate
Deleted: of the same attractor.

Deleted: separate

Deleted: in

Deleted: The

Deleted: introduced here

Deleted: current

Deleted: time.

a.	If we cannot find seven unique ridges, use as many unique ridges as we can, and separate ridges into intersections with latitude bands. Find points closest to our subdivided ridges.
4)	If specified, restrict neighbourhood of ridges to that which intersects with neighbourhood of airports.
5)	Identify the points with the highest DBS_{FW} value for each neighbourhood and select the highest seven.
Output: Seven aerosol injection locations optimized for the wind flow on day t_0	

290 **Table 1: Summary of the method of identifying injection locations for DBS-informed injections.**

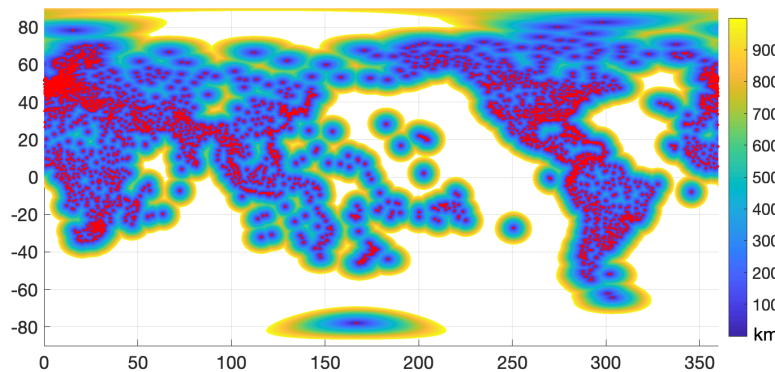


Figure 5: Global coverage of potential injection locations for an airport-bound scenario including a map of 9300 airport locations (red dots) and the distance to the nearest airport up to 1000 km.

Deleted: 4

295 As a control study, we ran a baseline scheme that injected sulfate aerosols at seven fixed-injection locations referred to in the text as FI, $(0, \pm 15, \pm 30 \text{ and } \pm 50^\circ \text{ latitude at } 260^\circ \text{ longitude})$ similar to those explored by others [e.g. Robock et al., 2008; Heckendorn et al., 2009; Tilmes et al., 2017]. Lastly, we ran a scenario where DBS injections were restricted to within 1000 km of an airport (scenario ADI in the text) [Global Airport Database, 2020] as a logistical handicap more similar to real world possibilities (Figure 5). For both the unrestricted DBS and the airport protocols, we limited the selection of injection locations to latitudes between $\pm 62.5^\circ$ to avoid trapping by meridional barriers near the poles [Beron-Vera et al., 2012] while maximizing 300 global coverage. Despite this restriction, the stratospheric flow sufficiently mixed aerosols across the globe, as with the FI experiments.

Deleted: We compared our DBS injection scheme to

Deleted: the

Deleted: injection site had

Deleted: be

Deleted: 4

Deleted: and maximize

Deleted: is still able to mix particles to higher latitudes (Figures 3 and 5).

2.3 Geoengineering performance metrics

For our basic dispersion analysis, we evaluated the effective global coverage and rate of dispersion via an average minimum-distance metric defined as

$$\mu(t) = \frac{1}{N} \sum_{x \in D} \min(d(x, \gamma(t))), \quad (1)$$

315 where $x \in D$ are all points on the globe, d is the great-circle distance, $\gamma(t)$ is the location of all ~~neutral (aerosol)~~ tracers at time t , and N is the number of grid points on the globe used for the calculation. Lower values of μ indicate a shorter distance from any point on the globe to the nearest aerosol, and thus imply better coverage. As volumetric or mass concentrations of aerosols are driving factors in many of the microphysical processes governing aerosol lifespan, we also calculated the entropy of the distribution of ~~the pseudo-aerosols in our infinitesimal neutral tracer experiment. For a given probability p_k on a discretized~~

320 grid of (unequal) bins (such as tracer concentration).

$$E = - \sum_{x \in D} p_k \log_2 \left(\frac{p_k}{w_k} \right), \quad (2)$$

where w_k is the size of a bin [Harris, 2006]. The evolution of the entropy of each injection protocol was normalized by the entropy of a perfectly uniform distribution ~~on the same discrete grid to give a normalized entropy value in the interval [0, 1]~~.

At the beginning of each month during the 18.75-year CESM2 simulation, we initiated advection of fluid-following neutral tracers from seven DI sites, seven ADI sites, and seven FI sites that lasted for 50 weeks. In these initial experiments, we did

325 not ~~run a new simulation of CESM2(WACCM6), but used the advection of neutral tracers in wind fields generated by CESM2(WACCM6) (Run #1) to approximate the dispersion dynamics of aerosols in a fully turbulent stratosphere (left column of Figure 3)~~.

In our second ~~round of experiments~~, we used ~~the~~ precomputed wind fields from CESM2 Run #1 to determine injection sites, and then ~~ran~~ new CESM2 simulations starting in each season (Run #2) with 10 Tg SO₂ injections that included fully-coupled

330 microphysics. In this way, the atmosphere was influenced by geoengineering in Run #2, but not in our neutral-tracer experiments. The effective global coverage, SO₄ burden, and effective radii were then compared for the two DBS-informed (DI and ADI in the text) and one fixed (FI) injection protocols.

3 Results

3.1 DBS influence on aerosol dispersion

For the ~~infinitesimal neutral-tracer~~ advection experiment (Figure 3, left column), the global coverage of ~~pseudo-aerosols~~ injected at seven dynamically varying ~~DBI~~ locations was much greater than coverage from the seven fixed (FI) locations. We found an immediate increase in global coverage for the ~~DI experiments~~, as predicted from the mathematical definition of large DBS_{rw} values. ~~Zonal~~ concentrations of ~~tracers~~ were calculated as the fraction of the total number of ~~tracers~~ present in a given 340 discrete latitude band.

Deleted: aerosols
Deleted: aerosol concentrations
Deleted: in
Deleted: $E = - \sum_{x \in D} p_k \log_2 \left(\frac{p_k}{w_k} \right)$
Deleted: of aerosols
Deleted: relative
Deleted:
Deleted: We compared
Deleted: cumulative coverage
Deleted: injections using
Deleted: DBS-informed locations (with and without airport restrictions) and
Deleted: fixed-locations
Deleted: up to
Deleted: of advection over the entire 18.75-year simulation period. In this
Deleted: experiment
Deleted: inject aerosols into
Deleted: computed
Deleted: fluid particles
Deleted: experiment
Deleted: recomputed a
Deleted: simulations, where
Deleted:
Deleted: increase in airborne H₂SO₄ mass, and the lifespan of the
Deleted: three
Deleted: The effective lifespan was calculated as the first instant
Formatted: Normal
Formatted: Font: Bold
Formatted: Font: Bold, English (UK)
Deleted:
Deleted: simulation without microphysics,
Deleted: (DBS-informed) injection
Deleted: -injection
Deleted: DBS-informed injections
Deleted: Figures 5a and 5c detail how the zonal
Deleted: ideal sulfates injected at
Deleted: standard fixed-locations evolve over the first seven days
Deleted: the volume of particles, there is little-to-no dispersion
Deleted: the bottom two subplots of Figure 5.

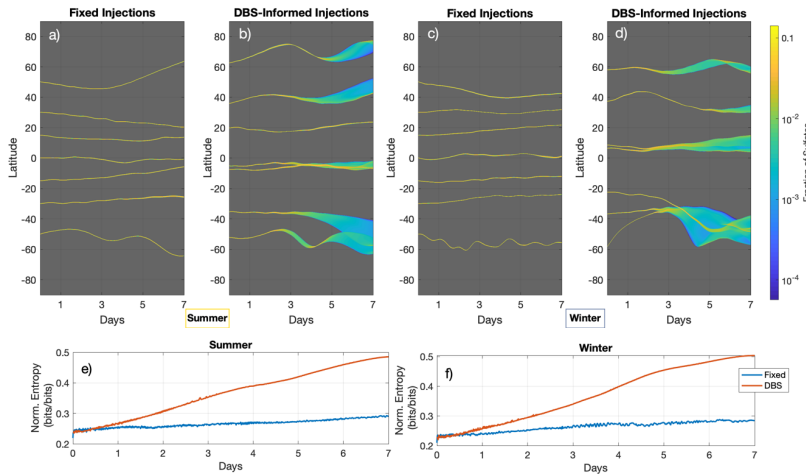
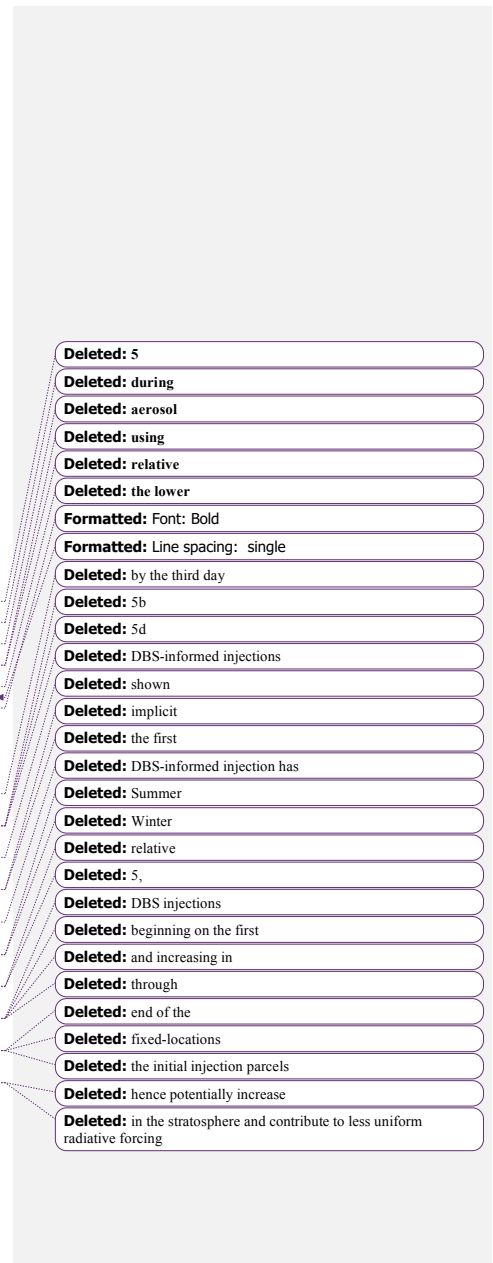


Figure 6: DBS-informed injection yields significantly enhanced coverage over fixed-location injections over short-term, seven-day periods. Zonal concentrations in subplots a-d are calculated as the fraction of the total number of neutral-tracers in a given latitude band at a given time. The time evolution of zonal concentration over one week of transport from the two injection protocols are displayed in subplots a-d with their respective normalized entropy values in subplots e-f.

395

Figures 6a and 6c detail how the zonal concentrations of these idealized sulfates injected at the standard FI sites evolve over the first seven days of transport during boreal summer and winter, respectively. While there is North-South meandering of the injected tracers, the fixed-injection scheme resulted in little-to-no dispersion by the end of the first week. In contrast, after only 400 three days of transport, Figure 6b and 6d show that the DI tracers have begun efficiently spreading and increasing global coverage. As is discussed later and exhibited in the full microphysics simulations in the next section, this immediate dispersion has an impact on the rate of coagulation, sedimentation, and the effective radii and lifespan of the aerosols. By the end of seven days, the DI tracers have covered a large portion of the northern and southern hemispheres from -70° to 70° for both the summer and winter injections. This difference in global coverage between DI and FI schemes is further quantified by the 405 normalized entropy of aerosol distributions for the two protocols. In the bottom two subplots of Figure 6 (6e and 6f), the aerosol distribution from the DI protocol has greater entropy (Eq. 2) after one day of transport with that performance gap widening for the entire week. At the same time, the near constant entropy for the FI experiments verifies that those clusters of neutral tracers have not yet dispersed, and create a longer window of time for sulfate “hot-spotting” and coagulation.



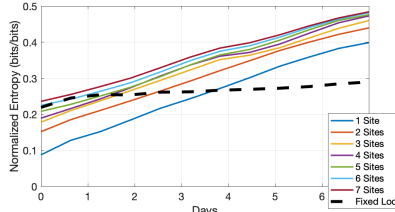


Figure 7: Normalized entropy of DBS-informed injections under a varying number of sites for the summer simulation in Figure 6. Through optimizing injections near dispersion enhancing transport barriers, we are able to achieve significantly more uniform distributions of aerosols with fewer necessary injection sites.

The enhanced dispersion, made possible by harnessing DBS information, also allows for a streamlining of injection operations.

Using the same time period from Figure 6a-b, we were able to leverage the improved distributions of aerosols and test how reducing the number of DBS injection sites would influence the subsequent global coverage. Figure 7 shows that for one such

test, almost immediately, there is a negligible reduction in entropy when reducing from seven DBS-informed injections to six.

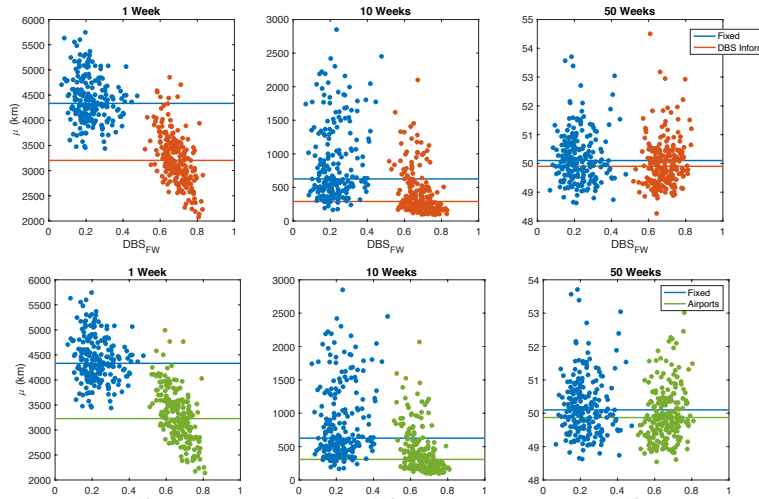
That is, within the first day of dispersion, reducing the number of injection locations, and the amount of injected material by nearly 15% does not impair the performance of our DBS protocol to levels below that of the fixed locations. After three days, when the influence of strong DBS barriers has been more effective, one can reduce injections to only two DI sites and still obtain a more uniform concentration distribution than with seven FI sites. From four days to the end of the first week, a single injection site was dispersing aerosols in the stratosphere more effectively than the combination of all seven fixed sites. Not only could a well-informed choice of injection locations provide significant benefits for increasing concentration homogeneity (thereby more evenly influence radiative forcing and reduce hot-spotting), there can be significant strategic and economic advantages of DBS-informed geoengineering programs.

To determine if injecting at DI sites would consistently increase dispersion over all seasons, and over many years, we consider the cumulative statistics of many long-term advection models. At monthly intervals, the same seven-day reanalysis and forecast method was used to choose DI locations, both with and without a 1000 km distance restriction to the nearest airport (ADI). After 1 week, 10 weeks, and 50 weeks of transport, μ values (Eq. 1) were computed and compared to the FI protocol. Figure 8 shows the results of this experiment for transport periods spanning the whole 18.75 years. Clusters of μ values indicate variance in the response of aerosol transport to different DBS ridge structures over time, but mean values of those clusters (indicated by horizontal lines) consistently show improved coverage compared to the FI protocol. As noted before, the most considerable enhancement in dispersion was seen immediately, supporting a probable influence on aerosol microphysics during the first week of transport. After 10 weeks, DI injections were still more effective at global coverage than the FI protocol,

- Deleted: <object>
- Deleted: 6: Relative
- Deleted: 5
- Deleted: <object><object>Figure 7
- Moved down [1]: : Average distance to nearest aerosol (Eq. 1) with injections initialized each month for 18.75 years.
- Deleted: The top three subplots compare the fixed location protocol to the DBS informed injection after 1 week, 10 weeks and 50 weeks of transport, with cluster means marked by respective horizontal lines. The bottom three subplots are ... [5]
- Moved down [2]: Both DBS approaches outperform the fixed
- Deleted: simplification
- Deleted: 5a
- Deleted: enhanced concentration
- Deleted: aerosol
- Deleted: 6
- Deleted: relative
- Deleted: a near 15% reduction in
- Deleted: and injection sites
- Deleted: reduce
- Deleted: have
- Deleted: reducing injection
- Deleted: DBS-informed locations
- Deleted: resulted in
- Deleted: the
- Deleted: fixed locations. After
- Deleted: The advantages of
- Deleted: location could thus
- Deleted: benefit to
- Deleted: and heterogeneous radiative forcing, as well as reduce [6]
- Deleted: burden
- Deleted: a
- Deleted: program
- Deleted: DBS-informed injections
- Deleted: DBS-injections
- Deleted: .
- Deleted: fixed-injection
- Deleted: 7
- Deleted: fixed
- Deleted: DBS-informed
- Deleted: fixed-location

even with the airport restrictions, but at yearly timescales, the average improvement was minimal. It should be noted that the variance of global coverage was also lowest for DI seeding at 10 and 50 weeks.

Deleted: DBS-informed



520 **Figure 8:** Average distance to nearest aerosol (Eq. 1) with injections initialized each month for 18.75 years. The top three subplots compare the fixed location (FI) protocol to the DBS-informed (DI) injection after 1 week, 10 weeks and 50 weeks of transport, with cluster means marked by respective horizontal lines. The bottom three subplots are analogous with the added restriction that DBS informed injections must also be within 1000 km of an airport (ADI). Both DBS approaches outperform the fixed injections protocols up to 10 weeks, suggesting flexibility of the protocols and utility of harnessing Lagrangian coherent structures for enhancing dispersion.

525

3.2 Full atmospheric chemistry and microphysics simulations

Beyond improved advective transport of aerosols, we also wish to investigate the role that diffusion transport barriers may play in dampening microphysical processes that can reduce the lifespan of geoengineering aerosols, such as coagulation and sedimentation, in a fully coupled climate model. To address this, we applied the DI and ADI site selection methods at the 530 beginning of four months (January, April, July, September) during one year of CESM2(WACCM6) output. We then reran twelve CESM2(WACCM6) simulations with injections of 10 Tg of SO₂ for the three separate protocols, on a given day, t_0 , in each season. For each model run, the SO₂ was divided evenly between the seven fixed or dynamic injection sites on the 540 K isentrope. This provided twelve year-long model simulations that calculated the total evolution of injections from each geoengineering protocol. The average effective radii of sulfate aerosols, total column SO₄ burden (kg/m²), and top-of-

Moved (insertion) [1]

Moved (insertion) [2]

Deleted: selected

Deleted: DBS-informed

Deleted: airport-restricted DBS-informed location

Deleted: from

Deleted:

Deleted: For each t_0 we

Deleted: the

Deleted:

Deleted: model from t_0 forward

Deleted: after injecting 10 Tg of SO₂

Deleted: single

Deleted: spread

Deleted: across

Deleted: resulted in

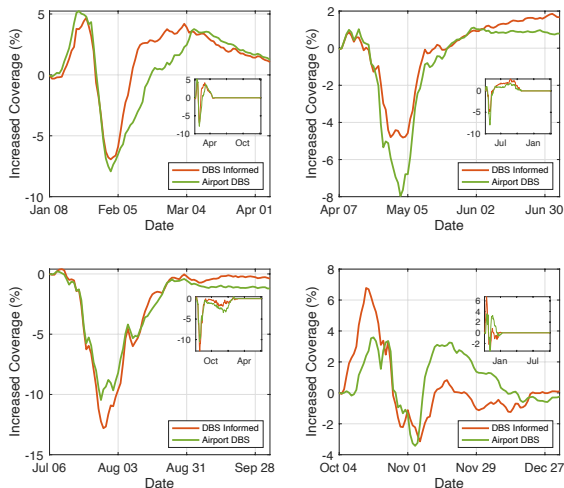
Deleted: calculate

Deleted: The mol/mol concentrations of H₂SO₄

atmosphere radiative forcing was measured on a lat-long grid over isentropes from 360 to 720 K. The seasonal experiment names referred to in this section correspond with the boreal season.

555 3.2.1 Aerosol Burden

As DBS ridges and this particular coherent structure view of stratospheric dynamics are mathematical tools to address dispersion and transport, we initially focus on enhancements in SO_4 dispersion and global coverage when using DBS-informed site selections. To account for the natural variability of SO_4 burden in our control runs, effective coverage was quantified from the cells whose total column SO_4 burden exceeds five times the average global burden for the one week prior to sulfate injection. The amount of global coverage is then the percent of the surface area of the earth with SO_4 exceeding this threshold. Around 1% of the surface area of the earth exceeds this threshold prior to injection.



560 **Figure 9: Analysis of CESM2 (WACCM6) output showing the increase in percent of the Earth's surface surrounded by an SO_4 burden greater than five times the global mean from the week prior to injection as compared to fixed injection protocols. Large subplots show the first 90 days after injection and the smaller subplots show the first full year.**

Figure 9 shows the difference in global coverage between the DBS-schemes and the FI protocol. A consistent short-time pattern was evident in these time series for all four seasons' injection. There is an immediate positive difference with the DBS approaches as a greater percent of the Earth is efficiently covered by an above-average SO_4 burden. This initial improvement

Deleted: nineteen

Deleted: spanning

Deleted: The first notable finding is the increase in the lifespan of the aerosols for the DBS-informed and airport-restricted injection protocols. Each subplot in Figure 8 details the evolution of the total mass of the modeled H_2SO_4 in the atmosphere, as compared to pre-injection values, for one year. The date at which the H_2SO_4 mass returned to within 10% of pre-injection values is marked for each protocol with a vertical dashed line. For each of the four seasons of injection, the two DBS-informed protocols enhanced the lifespan of aerosols and increased the impact of geoengineering as compared to the standard fixed-location approach. The largest increases in lifespan, those from injections in April, were evenly split for the Northern and Southern hemispheres. The second largest increase in lifespan (October injections) was largely caused by prolonged transport in the Southern hemisphere. On average these improvements resulted in a 22.5 day increase in the lifespan of aerosols for the unrestricted DBS-informed method and a 24.5 day increase in lifespan for injections with the 1000 km airport restriction. The extended lifespan after imposing the airport restriction is due to the chaotic three-dimensional nature of atmospheric flows and influence of long-time flow evolution that is unknown for the seven-day isentrope-restricted DBS calculations. Spikes in H_2SO_4 mass that occur after the initial injection peak are the result of the vertical transport of modeled aerosols moving back into the measurement domain, e.g., crossing the 360 K or 720 K isentropes. ¶

<object> ¶

Figure 8: Calculation of H_2SO_4 mass evolution in CESM2 (WACCM6) simulations for sulfate precursor injections during four seasons. Vertical dashed lines indicate the first day at which the total mass of H_2SO_4 returned to within 10% pre-injection values for the three injection protocols. ¶

We also analyzed the effective global coverage of each injection protocol (Figure 8). This was calculated by projecting the concentration of H_2SO_4 on each isentrope onto the earth's surface, and finding the fraction of the earth's surface area for which the mass of H_2SO_4 was greater than the global pre-injection mean. While the short-term improvements in coverage and distribution has been thoroughly discussed in Section 3.2, it is important to note that at yearly timescales, coverage by the DBS-informed and airport-restricted methods was better than the fixed protocol up to 75% of the time. To put it another way, while we identified the most important diffusive transport barriers for one week of idealized isentrope-restricted transport with no guarantees on longer behavior, the lasting presence and influence of these coherent structures is evident up to a year later. Figure 10 confirms the advantages of a variable seeding method, showing that stratospheric sulfate aerosol size is generally smaller for the DBS seeding schemes than the fixed schemes.

in coverage peaks between one week and two weeks after injection and is attributed to high DBS_{FW} values at injection locations and an enhanced ability to strategically spread along nearby jets and eddies that were present in the DBS_{BW} fields. These dispersion patterns and their correlation with DBS_{BW} ridges can be seen in the SO₄ burden plots of Figure 10. This immediate improvement can be as high as 5% more global coverage, equating to a change in net radiation over an additional 32 million

625

km², or more than the equivalent surface area of North America.

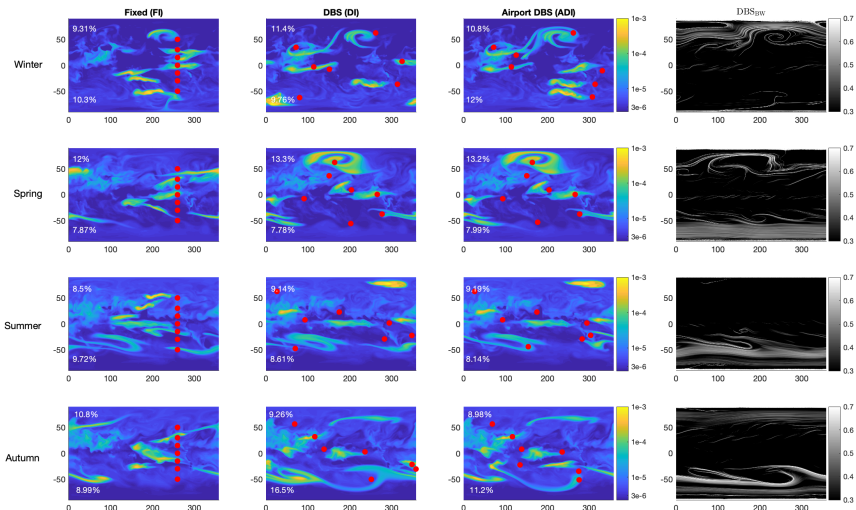


Figure 10: Analysis of CESM2 (WACCM6) output showing the SO₄ burden after seven days of transport for the three injection protocols in each season. The percent of the earth's surface covered by an SO₄ burden greater than the global mean from the week prior to injection is noted in the top left of each panel. Original injection locations for each experiment are shown as red dots. Units for the colormap are kg m⁻².

630

After the initial peak improvement in global coverage, there is often a rebound in Figure 9, at which point the F1 aerosols can cover up to 12% more of the globe. Surprisingly, after this local minimum, there is always a secondary peak, sometimes larger than the first, showing a response in global coverage using the DBS methods well past the computational limitations of the

635

original DBS ridges. This second peak in performance occurs between six and ten weeks after injection, and enhanced coverage by the DBS methods can extend until all three experiments achieve total global coverage.

Notably, the spring and summer season injections had much smaller relative improvements in their initial peaks in Figure 9. A closer investigation of the dispersion patterns in Figure 10 begins to explain why. The left three columns of Figure 10 show the SO_4 burden with the two inset percentages in each plot detailing the proportion of the respective hemisphere's (North or

640 South) surface area covered by five times pre-injection burden means. The right column shows the DBS_{BW} field calculated for the 540K isentrope wind fields from the injection time t_0 to $t_0 + 7$ days so that the location of attracting structures coincides with the concurrent dispersion patterns. The winter injections occurred in the presence of strong attracting features in most latitude bands, and the DBS-informed methods were able to exploit these, especially in the northern hemisphere. Dispersion along these attracting features continued to enhance coverage for DI and ADI injections well after the snapshot in

645 Figure 10. During spring, the DBS-informed injections exploited the similar attracting features in the northern hemisphere (13% vs. 12% coverage) but in the southern hemisphere, attracting ridges around -50° blocked aerosols from migrating further south in all three experiments.

The summer injections occurred during an absence of strong attracting or repelling structures, except a dominant circumpolar feature in the southern hemisphere. The DBS_{FW} values for sites chosen north of -37.5° for the summer DI and ADI experiments

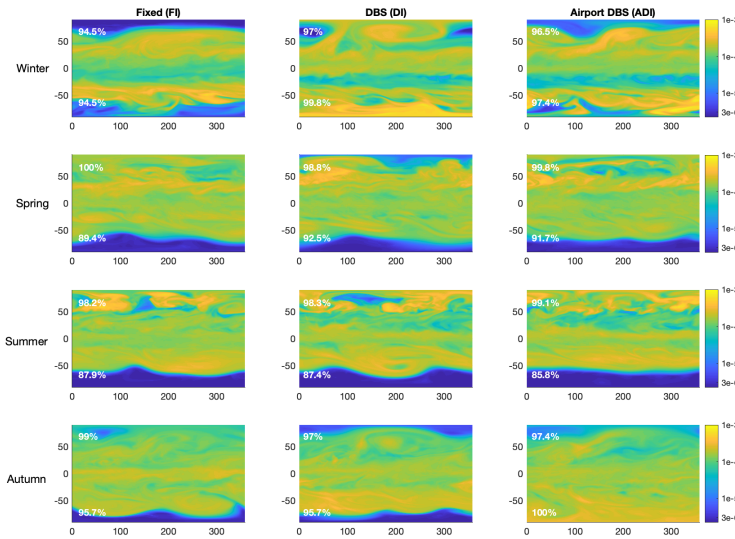
650 were the lowest of all the experiments. In the northern hemisphere, aerosols spread by way of these locally maximal DBS_{FW} injection sites, but no strong anticyclonic structures, such as those found in the other seasons, were present. This prevented northern hemisphere aerosol clouds from deforming along space-filling spiral features such as in the south and in other seasons.

The autumn injection occurred during a time with stronger DBS_{FW} and DBS_{BW} ridges than the summer injection, and allowed for an enhanced dispersion in the south, especially for the DI experiment. The true strength of the DBS approach can be seen

655 in the autumn experiment as only minor modifications in the southern hemisphere were necessary to achieve considerable enhancement in coverage. After seven days, DI SO_4 burden was above our threshold for 21% of the globe, versus only 16% from FI. This advantage comes solely from enhanced performance in the southern hemisphere where DI coverage was 13.4% and FI lagged at 6.8%. This significant advantage came from only a minimal change of injection point. The southernmost DI site was 0.25 degrees latitude further south than the FI site, and less than 650 km away, but the presence of strong DBS_{BW}

660 ridges, and complementary high DBS_{FW} values allowed for a beneficial optimization.

Figure 11 details the SO_4 burden after eight weeks of transport. At this point, during the last oscillation of Figure 9 prior to total coverage, the three injection techniques begin to converge. Notable exceptions to this are the enhanced polar coverage in the winter DI injection in the autumn ADI experiment.



665 **Figure 11: Analysis of CESM2 (WACCM6) output showing the SO₄ burden after eight weeks of transport for the three injection protocols in each season. The percent of the earth's surface covered by an SO₄ burden greater than the global mean from the week prior to injection is noted in the top left of each panel. Units for the colormap are kg m⁻².**

670 **3.2.2 Effects on Radiative Forcing**

The dispersion patterns caused by the hyperbolic coherent structures in the stratosphere discussed in the previous section impacted the top-of-atmosphere radiative forcing (RF) in a complex way. The net shortwave and longwave fluxes were calculated for each grid cell on each day, as were the radiative fluxes for a control run over the same period without geoengineering. The control fluxes were then subtracted from net fluxes to give a spatial and temporal distribution of the

675 relative influence of each injection scheme. This change in RF is directly correlated with a change in temperature and is a strong indicator of the climatic influence of geoengineering [Hansen et al., 1997; Gregory et al., 2004].

Comparing the global effect of the FI protocol with DI and ADI, we find the cumulative impact of the DI and ADI injection was stronger in many cases. Table 2 shows the mean global change in RF for each injection protocol, during each experiment, after three periods of time (10 days, 30 days, 365 days), calculated as the average difference in net radiation at the respective

680 time after injection. The three values in each column correspond to the global average FI (black), DI (orange), and ADI (green) difference from the control run in W m^{-2} . Gray shaded cells indicate times at which FI resulted in stronger radiative forcing than DI and ADI. Bold DI and ADI values indicate a statistically significant difference (at 95%) in RF from the FI protocol using a two-sided *t* test.

	10 Days	30 Days	365 Days
Winter	-1.4/-2.0/-1.7	-6.9/-5.0/-6.2	-7.6/-3.6/+0.4
Spring	-1.1/-1.3/-2.0	-7.6/-6.7/-6.1	-11.1/-11.2/-9.6
Summer	-1.5/-1.2/-0.8	-4.0/-6.1/-6.6	-3.4/-3.0/-2.0
Autumn	-1.5/-2.0/-2.0	-10.1/-10.4/-11.2	-9.9/-11.1/-4.6

685 **Table 2: Global average improvement in RF (W m^{-2}) at specified intervals after injection as compared to CESM2(WACCM6) control runs for FI (black), DI (orange), and ADI (green) injection schemes. Bold values indicate a statistically significant difference in mean RF between FI and the corresponding DBS-informed injection on that day. Gray shaded cells indicate times at which FI resulted in stronger RF than both DI and ADI.**

690 Over the first ten days of transport, the range of time for which our DBS methods can be mathematically supported, both global coverage and RF was often improved with DBS-informed injection. As could be expected from Section 3.2.1, there was a reduction RF for summer DI and ADI experiments. This corresponds with a lack of attracting and repelling structures, and questionable conditions for which to apply our injection site selection algorithm. After 30 days, only winter and spring RF for FI outperformed DI or ADI. This is during the rebound period detailed in Figure 9. At this point, well beyond the time horizon 695 of our DBS calculations, summer and autumn DI and ADI had stronger RF than FI. After 365 of transport, FI outperformed the DBS protocols for the winter and summer injections. At these time scales it can be safely assumed that the chaotic nature of stratospheric winds prevents any intelligible dependence on initial conditions for these injection experiments. There exists a complex nonlinear relationship between global coverage and RF, however, during the forecast windows we have investigated, there is a strong correlation between the enhanced dispersion from DBS-informed injections and RF. For longer 700 term trends, one likely needs to be couple short time dispersion with other influential climatic variables, such as season of injection (e.g. Visoni et al., 2020).

3.2.3 Aerosol Effective Radii

705 The last metric from the geoengineered CESM2 simulations we analyzed is the effective radius of aerosols (Figure 12). The time evolution of the mass-averaged SO_4 aerosols was calculated on the 540 K isentrope, at the height where injection occurred. To prevent contributions of naturally occurring aerosols, the averages were calculated only using grid cells where the SO_4 burden exceed five times the pre-injection mean. During the winter season, the most dramatic change in radii occurred, with peak values for the simple injection protocol clearly exceeding the DI and ADI methods. Differences in other seasons were more minor, but the injection protocol peaked at higher values for both the spring and autumn experiments as well. During

710 summer, there was reduced performance with the DBS-informed injections, as was also indicated in the RF and SO_4 burden analysis.

The improvement that was possible during the winter injection is notable as it suggests a better understanding of the connection between stratosphere dynamics and chemistry can clearly be beneficial for aerosol geoengineering. This is important because larger aerosols backscatter less (meaning more aerosol is required to achieve a given level of radiative forcing), heat the stratosphere more (resulting in greater side effects on stratospheric circulation and surface climate), and have increased sedimentation velocities (also meaning more aerosol is required) [Pierce et al., 2010; Tilmes et al., 2017; Simpson et al., 2019].

Deleted: <object>

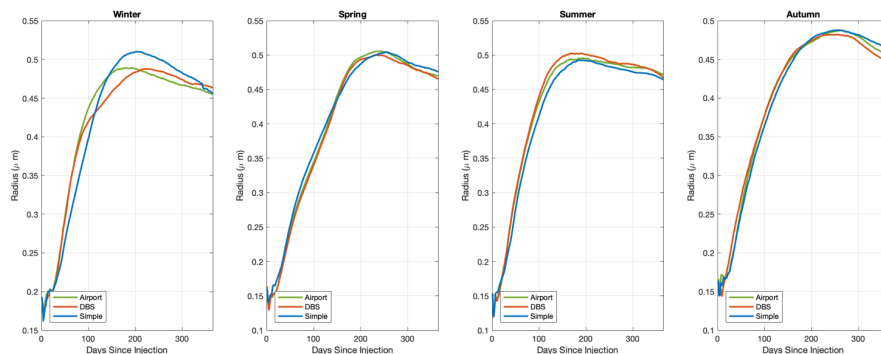


Figure 12: Mass-averaged effective radius of injected SO_4 aerosols on the 540 K isentrope spanning one year of CESM2(WACCM6) simulations after injection.

4 Discussion and Conclusion

720 Here we have explored the use of diffusive transport barriers to guide strategic injection locations for stratospheric aerosol geoengineering. Compared to commonly used methods that rely on fixed-injection locations, this dynamic site selection allows for immediate improvements in particle dispersion and better global coverage, often with fewer injection sites. This has important implications for previous studies regarding the efficiency of aerosol optical depth versus injection rate. In particular, by focusing on only fixed-injection locations [e.g. Robock et al., 2008; Tilmes et al., 2017 among others], these studies 725 neglected an influential variable, the time-varying locations of stratospheric diffusive transport barriers. It is safe to assume that since these studies did not optimize injections for dispersion, they have thus far underestimated what is possible for geoengineered sulfate-aerosols reflectance. Using a Lagrangian coherent structure informed approach via DBS fields shows great promise for strengthening the role that geoengineered aerosols can play in altering climate dynamics, especially at short timescales or if logistical restrictions mean injection sites must be strategically chosen.

730 With dynamic injection locations, initial particle concentrations spread much more quickly as indicated in our tracer experiments (Figures 6 and 8) and in the full CESM2 simulations (Run #2, Figures 10 and 11). This reduces the probability of

Deleted: 9: Analysis

Deleted:

Deleted: output showing the fraction of the earth's surface surrounded by a layer of H_2SO_4 of total mass greater than the global pre-

Deleted: mean.

Formatted: Font: Not Bold

Deleted: Page Break

<object>

Figure 10: Effective radius of geoengineering aerosols over the first 3 months of transport along the 540K isentrope. Note that the October injection resulted in a smaller effective radius for the fixed protocol and corresponds with the earlier peak in global coverage in Figure 9 and the higher total mass of H_2SO_4 in Figure 8.

<object>

Deleted: commonly used to study future climate scenarios

Deleted: injection

Deleted: ; in

Deleted:],

Deleted: appear

Deleted: the potential coverage and therefore reflectance of

Deleted: . This finding is three-fold justified by our work. First, with

Deleted: Figures 5 and 7, thus reducing

coagulation for each individual injection, and likely influenced lower peak effective radii present in DI and ADI experiments (Figure 12, e.g. Mills et al., 2017). With reduced coagulation, there will be slower descent of sulfates from the stratosphere (and out of action), as well as increased scattering. Second, increased dispersion uniformity, as quantified by normalized entropy in Figs 4 & 5, will reduce local stratospheric heating and result in more uniform radiative forcing. This is because heat transfer to aerosol particles in a given volume is proportional to the mass, which is reduced by lower concentrations. Lastly, in the fully-coupled CESM2(WACCM6) Run #2 experiments, DBS-informed injections improved global coverage by SO_4^4 . This ability to more quickly achieve total coverage provides opportunity to strategize geoengineering protocols with a shorter window for interference in chaotic flows.

The results here indicate a predictable enhancement of dispersion for geoengineering if influential hyperbolic structures are present in the stratosphere. When there are strong short-term DBS_{FW} and DBS_{BW} ridges, such as in the winter, spring and autumn CESM2 Run #2 experiments, we show that we can exploit these ridges to optimize the immediate dispersion of aerosols. As well, the fine scale behavior of aerosol dispersion can be explained by the presence of influential structures, such as the attraction and blocking that occurs in the southern hemisphere Run #2 spring experiment. These fine scale structures have not been actively considered in geoengineering research, but may be exploited as is clear in the northern hemisphere for the winter and spring experiments (Figure 10). In our fully-coupled microphysics and atmospheric chemistry climate simulations, we also verified that initial improvements in particle dispersion from simplified flow calculations can result in long-term gains in SO_4^4 burden and radiative forcing, and reduced effective aerosol radii. The enhanced global distribution of SO_4^4 for the two DBS-informed injection protocols after months of transport (e.g. Figure 11) speaks to the utility of strategic placement of aerosols near hyperbolic structures, as do long term radiative forcing improvements (Table 2), and correlated, yet complex, relationships with reducing average effective radii.

The extent of this influence is dramatically portrayed in the autumn CESM Run #2. At this time, a minimal modification of injection site in the southern hemisphere near strong hyperbolic structures, a change of less than 650 km, resulted in aerosols spreading over an additional 7.5% of that hemisphere after 7 days. After eight weeks, this immediate DI dispersion benefit was not as noticeable, but the ADI scheme still contributed to improved coverage over the FI aerosols. The enhanced coverage in the autumn experiment is furthermore coincident with a considerable improvement in RF for the DI experiments at 10, 30 and 365 days. Additionally, there was a minor but statistically significant reduction in average aerosol radii ($p < 1 \times 10^{-5}$) one year after SO_4^4 aerosol injection. At longer time scales for several of the other CESM2 Run #2 geoengineering experiments, the relationship between immediate enhanced dispersion, radiative forcing, and aerosol radii was less clear. For example, in spring, the ability to achieve global coverage and reduce radiative forcing at long timescales was best for the DI protocol, but there was not a similar improvement in average aerosol effective radius. In the winter DI simulation, there was a significant reduction in aerosol radius and improved coverage compared to FI, but there was a weaker effect on radiative forcing one year after injection.

This research has shown that adapting aerosol geoengineering injections methods by considering 2D Lagrangian coherent structures provides an obvious advantage for dispersion of aerosols by enhancing longer term dispersion dynamics from only

Deleted: .

Deleted: relative

Deleted: 3 &

Deleted: , hot spots,

Deleted: reduced concentration. Lastly, more uniform aerosol coverage, means more uniform radiative forcing, and a more effective geoengineering protocol

Deleted: the

Deleted: resulted in

Deleted: even after including all the complexities of full climate model. The prolonged presence of H_2SO_4 in the stratosphere

Formatted: Subscript

Deleted: speaks to a reduction in sedimentation rates. Additionally, after many

Deleted: , when the atmosphere was thoroughly mixed, there was still evidence of the

Formatted: English (UK)

Deleted: of our

short forecast data. All results in section 3.1 suggest DBS-informed sites reliably outperform fixed locations when considering aerosol dispersion along isentropes as is rigorously guaranteed in the DBS metric derivation. The site-selection algorithm 810 developed herein, however, does not consider the full three-dimensionality of stratospheric flows, or any knowledge about common meteorological and climatic features. Thus, the user-independent injection protocol does not always result in enhanced radiative forcing or global coverage when strong attracting and repelling features are not present in all regions, such as the summer experiments in CESM2 Run #2. With this in mind, we suggest that future injection experiments use DBS fields and diffusive transport barriers to constrain their choice of injection site, but allow for user intervention in the absence of such 815 strong dispersive ridges, and to consider other influential variables such as seasonality of injection (e.g. Visioni et al., 2020) and aerosol microphysics, such as temperature and humidity.

In one injection season (winter), there is an appreciable reduction in effective radius, and a more negligible effect in the others. This indicates that there is both potential for dynamic injection to result in smaller aerosols, and it suggests there is room for 820 improving our understanding of the role dispersive stratospheric dynamics play in aerosol coagulation. Future work along these lines may further improve upon the findings indicated here as well as help to understand the limits of what improvement in reducing aerosol size is still possible by considering time-varying small-scale turbulent features.

Related to this study is the proposed idea of direct injection of H_2SO_4 droplets, instead of SO_2 gas, which would ostensibly 825 create a more monodisperse particle distribution and thus delay coagulation [Pierce et al., 2010]. The long-term advection-only analysis in Section 3.1 applies more directly to H_2SO_4 injection, in that this proposed method already injects particles, albeit with non-obvious consequences for the resulting size distribution. Further investigation is warranted to understand the relative effects of this method vs the SO_2 injection simulated in our CESM2 (WACCM6) simulations, particularly if injection locations are chosen dynamically. This is especially important given the stratospheric chemistry involved in SO_2 injection, including the approximately one-month timescale of conversion from SO_2 to sulfate aerosols.

The results presented here are for a single model; different models will indicate different stratospheric features and thus 830 different transport barrier locations and strengths. Of key importance is that the long-term dispersion analysis and structure identification methodology relied on two-dimensional transport along isentropes. This method has proven to be successful for advancing the goals of optimizing sulfate precursor injections; a full three-dimensional computation of DBS fields would further improve the results. Upon review of the results, it appears there was an over emphasis on the ability to separate “unique” 835 attracting structures from the 2D isentrope data. With the automated algorithm defined in Table 1, pairs of injection sites were sometimes chosen to be close together as it appeared their injected aerosols would end up on separate structures. In fact, these features may have actually been connected along the third dimension. Additionally, long-term trends of SO_4 burden present in the stratosphere were mixed, suggesting further considerations of seasonality (e.g. Visioni et al., 2020) and consideration of what structure is likely being represented by a DBS_{bw} ridge (e.g. a jet stream, polar vortex, something much less substantial). Though not investigated in the present research, with the introduction of stratospheric heating, cross-isentropic flow is likely 840 to occur (e.g., vertical uplift from the heating), potentially justifying a three-dimensional analysis for the flows used here. Vertical transport of aerosol is likely inevitable, but a 3D DBS analysis would exponentially increase the complexity and the

Deleted: in the improved global coverage of H_2SO_4

Formatted: English (UK)

Deleted: seen in Figures 8 and 9

Deleted: of

Deleted: As this increase in complexity

computational costs of finding injection locations. The currently proposed isentrope method is found to be satisfactory as a benchmark improvement in injection protocols at little to no increased operational cost as there are clear advantages in the short-time dynamics using the DBS forecasts. One alternative improvement to 3D DBS fields would be simultaneous 2D analysis of structures on a range of isentropes.

Deleted: , the

850 Several studies have found that the injection rate of SO₂ is the limiting factor in geoengineering efficiency by increasing coagulation [Heckendorf et al., 2009; Niemeier et al., 2011; Niemeier and Timmreck, 2015]. These studies, however, have neglected to optimize the dispersion of SO₂ during the first days following injection. This oversight has inhibited the potential of sulfate injections and prevented optimal radiative forcing in model simulations. We conclude that the exploitation of readily available short-range wind forecasts and reanalysis is a catalyst that will allow better understanding of what can be achieved

855 with climate geoengineering. It is possible that one of the reasons the improvements seen here are not more drastic is the acute focus on the response to large individual injections, a method not commonly used. We ran simulations that included a single day of injection in an effort to demonstrate dispersion capabilities. As the ability DBS ridges to predict dispersion dynamics has now been shown, a logical next step is to pursue more climate focused studies, such as injecting less mass over many successive injections using concurrent predictions. While the use of DBS-informed injections does not address many of the 860 potential hazards of geoengineering [e.g. Robock et al., 2008; Heckendorf et al., 2009], it is a significant step forward towards assessing the feasibility of geoengineering to prevent the climate from crossing a critical tipping point.

Deleted: While this change in injection approach

Formatted: English (US)

Author Contributions

865 NA, BK, DG and GH contributed to the writing of this manuscript and analysis of results. NA and GH developed the experiment design and methods. BK performed all CESM6(WACCM) model simulations. NA performed all other tracer and DBS computations.

Deleted: 1
1

Acknowledgments

870 Support for B.K. was provided in part by the National Science Foundation through agreement CBET-1931641, the Indiana University Environmental Resilience Institute, and the *Prepared for Environmental Change* Grand Challenge initiative. The Pacific Northwest National Laboratory is operated for the US Department of Energy by Battelle Memorial Institute under contract DE-AC05-76RL01830. This research was supported in part by Lilly Endowment, Inc., through its support for the Indiana University Pervasive Technology Institute, and in part by the Indiana METACyt Initiative. The Indiana METACyt 875 Initiative at IU was also supported in part by Lilly Endowment, Inc. The ocean flow data used for Figures 1 and 2 can be obtained from AVISO (<http://www.aviso.oceanobs.com>).

References

Beron-Vera, F. J., M. J. Olascoaga, M. G. Brown, and H. Koçak (2012), Zonal Jets as Meridional Transport Barriers in the Subtropical and Polar Lower Stratosphere, *J. Atmos. Sci.*, 69(2), 753–767, doi:10.1175/JAS-D-11-084.1.

885 BozorgMagham, A. E., and S. D. Ross (2015), Atmospheric Lagrangian coherent structures considering unresolved turbulence and forecast uncertainty, *Commun. Nonlinear Sci. Numer. Simul.*, 22(1–3), 964–979, doi:10.1016/j.cnsns.2014.07.011.

Crutzen, P.J. Albedo Enhancement by Stratospheric Sulfur Injections: A Contribution to Resolve a Policy Dilemma? (2006), *Climatic Change*, 77(211), <https://doi.org/10.1007/s10584-006-9101-y>

Domeisen, D. I. V., Garfinkel, C. I., & Butler, A. H. (2019). The Teleconnection of El Niño Southern Oscillation to the 890 Stratosphere, *Reviews of Geophysics*, 5–47, doi.org/10.1029/2018RG000596

Driscoll, S., Bozzo, A., Gray, L. J., Robock, A., & Stenchikov, G. (2012). Coupled Model Intercomparison Project 5 (CMIP5) simulations of climate following volcanic eruptions. *Journal of Geophysical Research Atmospheres*, 117(17). <https://doi.org/10.1029/2012JD017607>

Garaboa-Paz, D., J. Eiras-Barca, F. Huhn, and V. Peérez-Múñoz (2015), Lagrangian coherent structures along atmospheric 895 rivers, *Chaos*, 25(6), doi:10.1063/1.4919768.

Gettelman, A. et al. (2019), High Climate Sensitivity in the Community Earth System Model Version 2 (CESM2), *Geophys. Res. Lett.*, 46(14), 8329–8337, doi:10.1029/2019GL083978.

Global Airport Database: <https://www.partow.net/miscellaneous/airportdatabase/index.html>, last access: 4 May 2020.

900 Gregory, J. M., Ingram, W. J., Palmer, M. A., Jones, G. S., Stott, P. A., Thorpe, R. B., ... Williams, K. D. (2004). A new method for diagnosing radiative forcing and climate sensitivity. *Geophysical Research Letters*, 31(3), 2–5, doi:10.1029/2003GL018747

Hadjighasem, A., and G. Haller (2016), Geodesic Transport Barriers in Jupiter's Atmosphere: A Video-Based Analysis, *SIAM Rev.*, 58(1), 69–89, doi:10.1137/140983665.

Haller, G. (2015), Lagrangian Coherent Structures, *Annu. Rev. Fluid Mech.*, 137–162, doi:10.1002/9783527639748.ch3.

905 Haller, G., D. Karrasch, and F. Kogelbauer (2018), Material barriers to diffusive and stochastic transport, *Proc. Natl. Acad. Sci.*, 115(37), 9074–9079, doi:10.1073/pnas.1720177115.

Haller, G., D. Karrasch, and F. Kogelbauer (2020), Barriers to the transport of diffusive scalars in compressible flows, *SIAM J. Appl. Dyn. Syst.*, 19(1), 85–123, doi:10.1137/19M1238665.

Hansen, J., M. Sato, and R. Ruedy, 1997: Radiative forcing and climate response. *J. Geophys. Res.*, 102, 6831-6864, 910 doi:10.1029/96JD03436.

Harris, B. (2006), *Encyclopedia of Statistical Sciences*, 2nd, vol. ed., edited by N. Balakrishnan, C. B. Read, and B. Vidakovic, Wiley, New York.

Heckendorf, P., D. Weisenstein, S. Fueglistaler, B. P. Luo, E. Rozanov, M. Schraner, L. W. Thomason, and T. Peter (2009), The impact of geoengineering aerosols on stratospheric temperature and ozone, *Environ. Res. Lett.*, 4(4), doi:10.1088/1748- 915 9326/4/4/045108.

910 Jaiser, R., K. Dethloff, and D. Handorf (2013), Stratospheric response to arctic sea ice retreat and associated planetary wave propagation changes, *Tellus, Ser. A Dyn. Meteorol. Oceanogr.*, 65, 1–11, doi:10.3402/tellusa.v65i0.19375.

915 Kashimura, H., M. Abe, S. Watanabe, T. Sekiya, D. Ji, John C. Moore, J. N. S. Cole, and B. Kravitz (2017), Shortwave radiative forcing, rapid adjustment, and feedback to the surface by sulphate geoengineering: Analysis of the Geoengineering Model Intercomparison Project G4 scenario, *Atmos. Chem. Phys.*, 18, 3339–3356, doi:10.5194/acp-17-3339-2017.

920 Knutson, B., W. Tang, and P. W. Chan (2015), Lagrangian coherent structure analysis of terminal winds: Three-dimensionality, intramodel variations, and flight analyses, *Adv. Meteorol.*, 2015, doi:10.1155/2015/816727.

925 Kravitz, B., D. G. MacMartin, M. J. Mills, J. H. Richter, S. Tilmes, J.-F. Lamarque, J. J. Tribbia, and F. Vitt (2017), First simulations of designing stratospheric sulfate aerosol geoengineering to meet multiple simultaneous climate objectives, *Journal of Geophysical Research: Atmospheres*, 122, 12616–12634, doi:10.1002/2017JD026874.

930 Kravitz, B. and D. G. MacMartin (2020), Uncertainty and the basis for confidence in solar geoengineering research, *Nature Reviews Earth and Environment*, 1, 64–75, doi:10.1038/s43017-019-0004-7.

Mills, M. J., Richter, J. H., Tilmes, S., Kravitz, B., MacMartin, D. G., Glanzville, A. A., ... Kinnison, D. E. (2017). Radiative and chemical response to interactive stratospheric sulfate aerosols in fully coupled CESM1(WACCM). *Journal of Geophysical Research: Atmospheres*, 1, 13061–13078. <https://doi.org/10.1002/2017JD027006>

Nakamura, N. (2008), Quantifying inhomogeneous, instantaneous, irreversible transport using passive tracer field as a coordinate. *Lect Notes Phys* 744, 137–144.

Niemeier, U., H. Schmidt, and C. Timmreck (2011), The dependency of geoengineered sulfate aerosol on the emission strategy, *Atmos. Sci. Lett.*, 12(2), 189–194, doi:10.1002/asl.304.

935 Niemeier, U., and C. Timmreck (2015), What is the limit of climate engineering by stratospheric injection of SO₂, *Atmos. Chem. Phys.*, 15(16), 9129–9141, doi:10.5194/acp-15-9129-2015.

Olascoaga, M. J., M. G. Brown, F. J. Beron-Vera, and H. Koçak (2012), Brief communication Stratospheric winds, transport barriers and the 2011 Arctic ozone hole, *Nonlinear Process. Geophys.*, 19(6), 687–692, doi:10.5194/npg-19-687-2012.

940 Pierce, J. R., Weisenstein, D. K., Heckendorn, P., Peter, T., & Keith, D. W. (2010). Efficient formation of stratospheric aerosol for climate engineering by emission of condensable vapor from aircraft. *Geophysical Research Letters*, 37(18), 2–6. <https://doi.org/10.1029/2010GL043975>

Rasch, P. J., P. J. Crutzen, and D. B. Coleman (2008), Exploring the geoengineering of climate using stratospheric sulfate aerosols: The role of particle size, *Geophys. Res. Lett.*, 35(2), 1–6, doi:10.1029/2007GL032179.

945 Robock, A., L. Oman, and G. L. Stenchikov (2008), Regional climate responses to geoengineering with tropical and Arctic SO₂ injections, *J. Geophys. Res. Atmos.*, 113(16), 1–15, doi:10.1029/2008JD010050.

Rutherford, B., G. Dangelmayr, and M. T. Montgomery (2012), Lagrangian coherent structures in tropical cyclone intensification, *Atmos. Chem. Phys.*, 12(12), 5483–5507, doi:10.5194/acp-12-5483-2012.

Serra, M., and G. Haller (2016), Objective eulerian coherent structures, *Chaos*, 26(5), doi:10.1063/1.4951720.

Formatted: German

Serra, M., P. Sathe, F. Beron-Vera, and G. Haller (2017), Uncovering the edge of the polar vortex, *J. Atmos. Sci.*, 74(11), 3871–3885, doi:10.1175/JAS-D-17-0052.1.

950 Simpson, I. R., S. Tilmes, J. H. Richter, B. Kravitz, D. G. MacMartin, M. J. Mills, J. T. Fasullo, and A. G. Pendergrass (2019), The Regional Hydroclimate Response to Stratospheric Sulfate Geoengineering and the Role of Stratospheric Heating, *J. Geophys. Res. Atmos.*, 124(23), 12587–12616, doi:10.1029/2019JD031093.

Tallapragada, P., S. D. Ross, and D. G. Schmale (2011), Lagrangian coherent structures are associated with fluctuations in 955 airborne microbial populations, *Chaos*, 21(3), doi:10.1063/1.3624930.

Tang, W., M. Mathur, G. Haller, D. C. Hahn, and F. H. Ruggiero (2010), Lagrangian Coherent Structures near a Subtropical Jet Stream, *J. Atmos. Sci.*, 67(7), 2307–2319, doi:10.1175/2010JAS3176.1.

The Royal Society (2009), *Geoengineering the climate: Science, Governance and Uncertainty Report*, The Royal Society, London.

960 Tilmes, S., R. Müller, and R. Salawitch (2008), The sensitivity of polar ozone depletion to proposed geoengineering schemes, *Science*, 320(5880), 1201–1204, doi:10.1126/science.1153966.

Tilmes, S., J. H. Richter, M. J. Mills, B. Kravitz, D. G. MacMartin, F. Vitt, J. J. Tribbia, and J.-F. Lamarque (2017), Sensitivity of aerosol distribution and climate response to stratospheric SO₂ injection locations, *J. Geophys. Res. Atmos.*, 122(12), 12,591–12,615, doi:10.1002/2017JD026888.

965 Visioni, D., D. G. MacMartin, B. Kravitz, J. H. Richter, S. Tilmes, M. J. Mills (2020), Seasonally Modulated Stratospheric Aerosol Geoengineering Alters the Climate Outcomes, *Geophys. Res. Lett.*, 47, doi: 10.1029/2020GL088337

Wang, N., U. Ramirez, F. Flores, and S. Datta-Barua (2017), Lagrangian coherent structures in the thermosphere: Predictive transport barriers, *Geophys. Res. Lett.*, 44(10), 4549–4557, doi:10.1002/2017GL072568.

Page 10: [1] Deleted **Aksamit** **2/8/21 12:59:00 PM**

▼.....

Page 10: [2] Deleted **Aksamit** **2/8/21 12:59:00 PM**

▼.....

Page 10: [3] Deleted **Aksamit** **2/8/21 12:59:00 PM**

▼.....

Page 10: [4] Deleted **Aksamit** **2/8/21 12:59:00 PM**

▼.....

Page 12: [5] Deleted **Aksamit** **2/8/21 12:59:00 PM**

▼.....

Page 12: [6] Deleted **Aksamit** **2/8/21 12:59:00 PM**

▼.....